scientific reports

Check for updates

OPEN

Wearable MXene-enhanced organic Bio-FET paper patch for glucose detection in sweat with pH and temperature calibration

Milad Farahmandpour[1,2] & Zoheir Kordrostami[1,2]✉

This paper proposes the design of organic Bio-FET sensors using paper as a substrate. Three different wearable biosensors have been engineered for the non-invasive monitoring of sweat biomarkers. The proposed sensors, which have a field-effect transistor (FET) structure, contribute to an array that is flexible, bendable, affordable, disposable, and biocompatible. The approach of drawing Organic FETs (OFETs) on paper using a paintbrush could successfully make cost-effective sweat biochemical sensors (glucose and pH Sensors) and biophysical sensors (temperature-sensor) which are versatile and sensors for real-time health monitoring. PDMS, PEDOT: PSS, and sensitive materials have been used as the oxide layer, source/drain electrodes, and the FET channel, respectively. The wearable glucose sensor utilizes a composite of copper oxide (CuO), carboxyl-functionalized multiwall carbon nanotubes (MWCNT-COOH), and Ti_3C_2 MXene (Ti_3C_2 MXene/CuO/MWCNT) as the channel material in its FET structure, enhancing its sensitivity and performance. Additionally, Ti_3C_2 MXene/MWCNT and Ti_3C_2 MXene/rGO/MWCNT composites were employed in the pH and temperature sensors, respectively, to enhance their functionality and performance. The proposed Bio-FETs are fabricated in three different designs: resistive, side-gated and back-gated structures, and their responses are compared and discussed. Continuous health monitoring is achieved through a fully integrated, disposable wireless device that combines glucose, pH, and temperature sensing. The fabricated Bio-FET exhibits high sensitivity and promising reproducibility, stability, and repeatability. To enhance precision, the proposed glucose sensor has been calibrated using real-time temperature and pH measurements.

Keywords BioFETs, Wearable sensors, Non-invasive, Drawing on paper, Sweat

Electronic devices can be used as the electronic skin (E-skin)-based wearable biosensors for sweat monitoring. Field-effect transistor (FET) biosensors stand out for their sensitivity, selectivity, and versatility in detecting a wide range of analytes. The utilization of paper as a substrate offers cost-effectiveness, biocompatibility, and ease of fabrication. The porous nature of paper provides an ideal environment for sample diffusion, enhancing the sensor's sensitivity and response time. The fabrication of FET biosensors on paper typically involves the deposition of semiconductor materials, such as nanomaterials or organic semiconductors, onto the paper substrate[1–12].

The incorporation of carbon nanotubes (CNTs) and graphene in wearable biosensors provides a conductive and sensitive platform for detecting various analytes in sweat owing to their remarkable characteristics such as substantial surface-to-volume ratios, effective immobilization of biomolecules, heightened sensitivity, biocompatibility, energy-Saving, and adaptability to microfabrication[13].

To enhance the sensing properties of the paper-based devices, we propose using Ti_3C_2 MXene. They are a class of two-dimensional transition metal-carbides. When Ti_3C_2 MXenes are added to the channel material in a FET, they improve the electronic properties, increase reactivity, and rise the sensitivity of the proposed sensors because of their high surface area. Ti_3C_2 MXenes are biocompatible and make the sensors faster because of their catalytic role in sensing[14,15]. We show that the composites including Ti_3C_2 MXenes improve the performance of the wearable sensors.

[1]Department of Electrical Engineering, Shiraz University of Technology, Shiraz, Iran. [2]Research Center for Design and Fabrication of Advanced Electronic Devices, Shiraz University of Technology, Shiraz, Iran. ✉email: kordrostami@sutech.ac.ir

We have categorized different types of sensors for body fluids sensing in Fig. 1. The sensors can be categorized into enzymatic and non-enzymatic. Recently non-enzymatic sensors have attracted extensive research interest due to their low cost, high stability, fast response, and low limit of detection (LOD). But they exhibit less sensitivity and selectivity compared to enzymatic sensors. Most of the commercial glucose sensors use electrochemical methods based on Glucose Oxidase (GOx) enzyme[16,17]. GOx is highly selective and sensitive towards glucose molecules and more stable than other enzymes. However, it loses its performance when the pH is below 2 or above 8 and can be irrevocably damaged at temperatures over 40 ^{0}C[18].

The sensors can also be classified into invasive, minimally invasive, and non-invasive. Currently, invasive monitoring is the most common method for glucose measurement[19–21]. However, non-invasive sensing is the best method for continuous and real-time monitoring of the blood molecules. It is also possible to obtain the blood molecules values indirectly from tears, saliva, interstitial fluid, and sweat[22–25]. According to the sensing mechanism, the biosensors are categorized into three main types: electrochemical[26–29], optical[30,31], and bioelectronic sensors[4,32,33].

The proposed glucose, pH, and temperature-sensors are fabricated on a paper substrate using a paintbrush dipped in ink. Detecting pH, glucose, and body temperature in wearable biosensors is crucial for comprehensive health monitoring and disease management[32,33].

The proposed FET sensors comprise these materials: PDMS, PEDOT: PSS, and MWCNT/graphene/MXene inks, serving as the oxide layer, source and drain electrodes, and channel, respectively. The channels of FET for Glucose-Sensor and pH-Sensor were created using Ti_3C_2 MXene/CuO/MWCNT and Ti_3C_2 MXene/MWCNT, respectively. Additionally, a Ti_3C_2 MXene/rGO/MWCNT composite was utilized as a channel of body temperature-sensor.

This work has led to the development of three-function, drawable-on-paper wearable bioelectronic sensors array capable of detecting glucose and pH levels in sweat and measuring the body temperature. All FET sensors utilize Ti_3C_2 MXene as the channel material due to its tunable properties, high surface area for interaction with biomarkers, high mobility, and rapid electrical charge transfer to the PEDOT: PSS source and drain electrodes, which is essential for modulating the current in the FET sensors.

For selective sensing of glucose, we incorporated Ti_3C_2 MXene/CuO/MWCNT. The addition of CuO to the Ti_3C_2 MXene channel facilitates the oxidation of glucose, producing electrons. MWCNT enhances the transfer of these released electrons to Ti_3C_2 MXene due to its ballistic properties, and ultimately allowing the electrons to be transferred to the PEDOT: PSS electrodes. For pH sensing, we used Ti_3C_2 MXene/MWCNT. The pure MWCNT and Ti_3C_2 MXene interact specifically with H + ions, enhancing the conductance of the p-type FET channel as H + ion concentration increases. Notably, glucose molecules do not undergo oxidation or reaction on the surface of the pure MWCNTs.

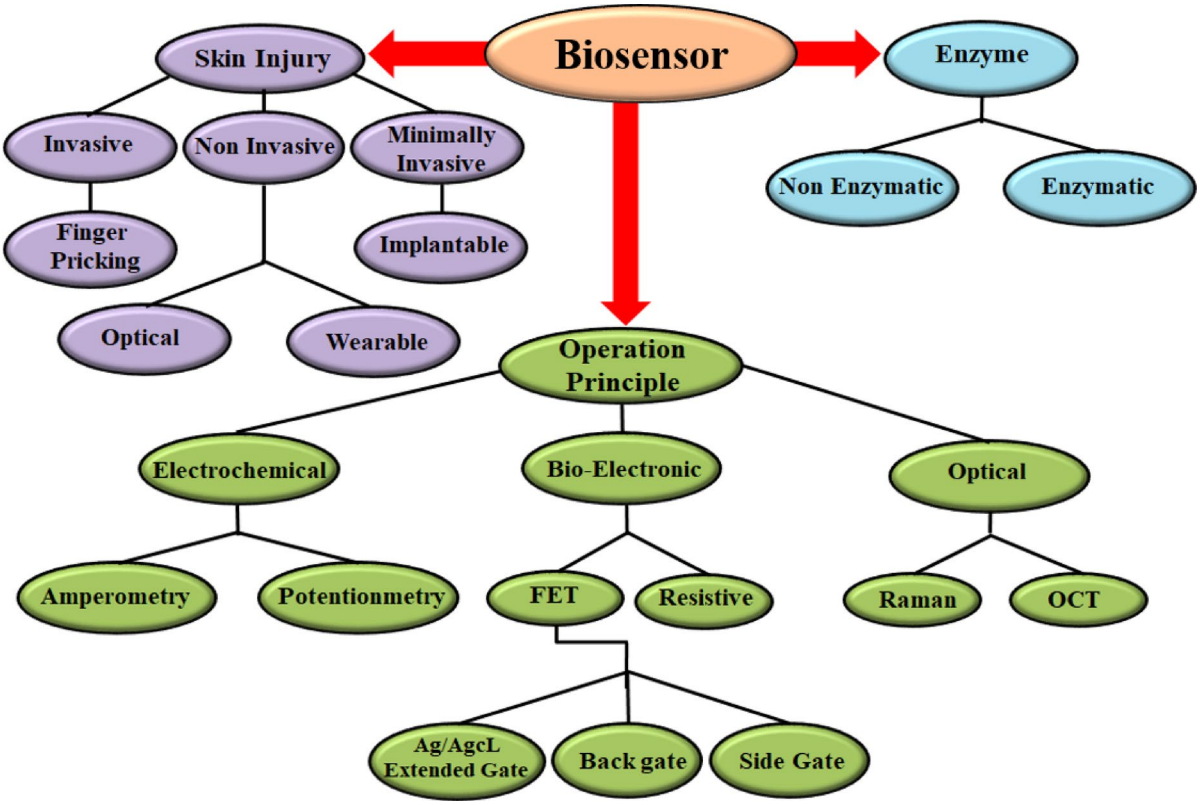

Fig. 1. Classification of the biosensor's detection methods.

For temperature sensing, we utilized Ti_3C_2 MXene/rGO/MWCNT due to its high electrical conductivity. As the temperature rises, the concentration of charge carriers in the Ti_3C_2 MXene/rGO/MWCNT composite increases, resulting in enhanced conductance of the p-type FET channel, where holes are the predominant charge carriers. The FET temperature sensor channel is coated with a thin layer of PDMS to prevent interference from sweat.

The E-skin FET biosensor

The FET biosensors can enhance the performance of monitoring sweat in the healthcare and fitness sectors, surpassing the performance of commercial three-electrode electrochemical sensors. Key features of the proposed electronic skin-based wearable biosensors include real-time, non-invasive, and customizable sweat monitoring based on biocompatible materials. The proposed FET biosensors operate based on electron transfer in p-type Ti_3C_2 MXene/MWCNT channel of a FET. The electronic skin is showcased in a innovative and futuristic manner where the proposed bioelectronics sensors are drawn on paper using ink-dipped paintbrush as shown in Fig. 2a. The gate electrode can be drawn on the paper on the same plane (side-gate) or can be drawn beneath the source and drain (back-gate). Figure 2b depicts a schematic of the sensors. Figure 2c presents a proposed wearable device seamlessly integrated with the skin. Visual representations demonstrate the different layers of the proposed wearable FET biosensor in Fig. 2d. Figure 2e and f, and 2g show images of the proposed schematic biosensor, a wireless, fully integrated disposable wearable device and a wearable biosensor attached on skin, respectively. The application of the smart phone can display the results of the measurements using IoT. Figures 2h shows electrical circuit diagram of the proposed wearable device.

Materials and apparatus

All reagents were procured from Sigma Aldrich and met analytical grade standards. The materials used in the study encompassed D (+) glucose (97%), Nafion, PDMS (Polydimethylsiloxane), phosphate-buffered saline (PBS), sulfuric-acid (H_2SO_4, 98%), nitric acid (HNO_3, 65%), multi-walled carbon nanotubes (MWCNT), CuO, PEDOT: PSS, lithium fluoride (LiF), HCl solution, Ti_3AlC_2, ethanol (96%), and sodium hydroxide (NaOH). The biosensors' sensitive material was formulated by blending Nafion (a sulfonated tetrafluoroethylene copolymer) with ethanol to generate a 5% solution in 96% ethanol, employing a 1:1 (wt %) ratio, and agitating for one minute. The PBS solution utilized possessed a concentration of 0.01 M and a pH value of 7.4. The Keithley 2450 source meter has been used for calculating I-V characteristics.

Fabrication process

Design and fabrication of paper electrodes

To create electrodes on paper using PEDOT: PSS (a conductive polymer with excellent electrical conductivity and stability), a drawing technique was employed. The electronic ink containing conductive polymer of PEDOT: PSS was deposited onto the paper substrate in a controlled manner to create the desired interdigitated electrode pattern by a paintbrush-dipped in ink. The ink was then dried to ensure adhesion and conductivity on the paper surface (For more detail see Figure S1 in the Supporting Information). Additionally, the choice of paper substrate can impact the adhesion, conductivity, and flexibility of the printed electrodes. Steinbach paper has been used as the substrate for developing the FETs. The drawn electrodes of the sensor on paper using PEDOT: PSS ink offers a cost-effective, lightweight, and environmentally friendly solution for creating flexible and wearable electronic devices.

Preparation of Ti_3C_2 MXene ink

Ti_3C_2 MXene was synthesized using the in-situ HF etching method. First, 1 g of lithium fluoride (LiF) powder was gradually added to 20 ml of a 9 M HCl solution and stirred for 30 min until fully dissolved. Following this, 1 g of Ti_3AlC_2 was introduced into the LiF/HCl mixture, which was then placed in an ice bath. The reaction was maintained at 50 °C for 48 h with continuous stirring. After the reaction period, the resulting black powder was collected by centrifugation and thoroughly washed with deionized water until the supernatant reached a pH of 6. Finally, the powder was dried under vacuum at 60 °C for 12 hours[34].

Preparation of MWCNT ink

To prepare CNT-based electronic ink, ultrasonic treatment is employed to disperse MWCNTs in 10 mg/ml of DI water. Subsequently, mixing in a stirrer helps to ensure uniform distribution of the CNTs within the ink solution[34].

Preparation of MWCNT-COOH ink

The functionalization of MWCNT starts with a mixture of nitric acid and sulfuric-acid in a 1:3 ratio. This process introduces carboxyl groups (COOH) onto the MWCNTs surfaces, enhancing their dispersibility and reactivity in biosensing applications. First, 50 mg of MWCNT is combined with the nitric-acid and sulfuric-acid mixture. The acids help to oxidize the CNTs and create defects on their surface, facilitating the attachment of functional groups. The resulting solution is subjected to ultrasonication for 30 min to disperse the CNTs and promote the reaction between the acids and the nanotubes, ensuring a more uniform functionalization. Next, the solution is maintained at a temperature of 50 °C for 6 h. After the reaction is complete, the functionalized CNTs are rinsed with deionized water to remove any residual acids or byproducts. The nanotubes are then dried to remove excess water.

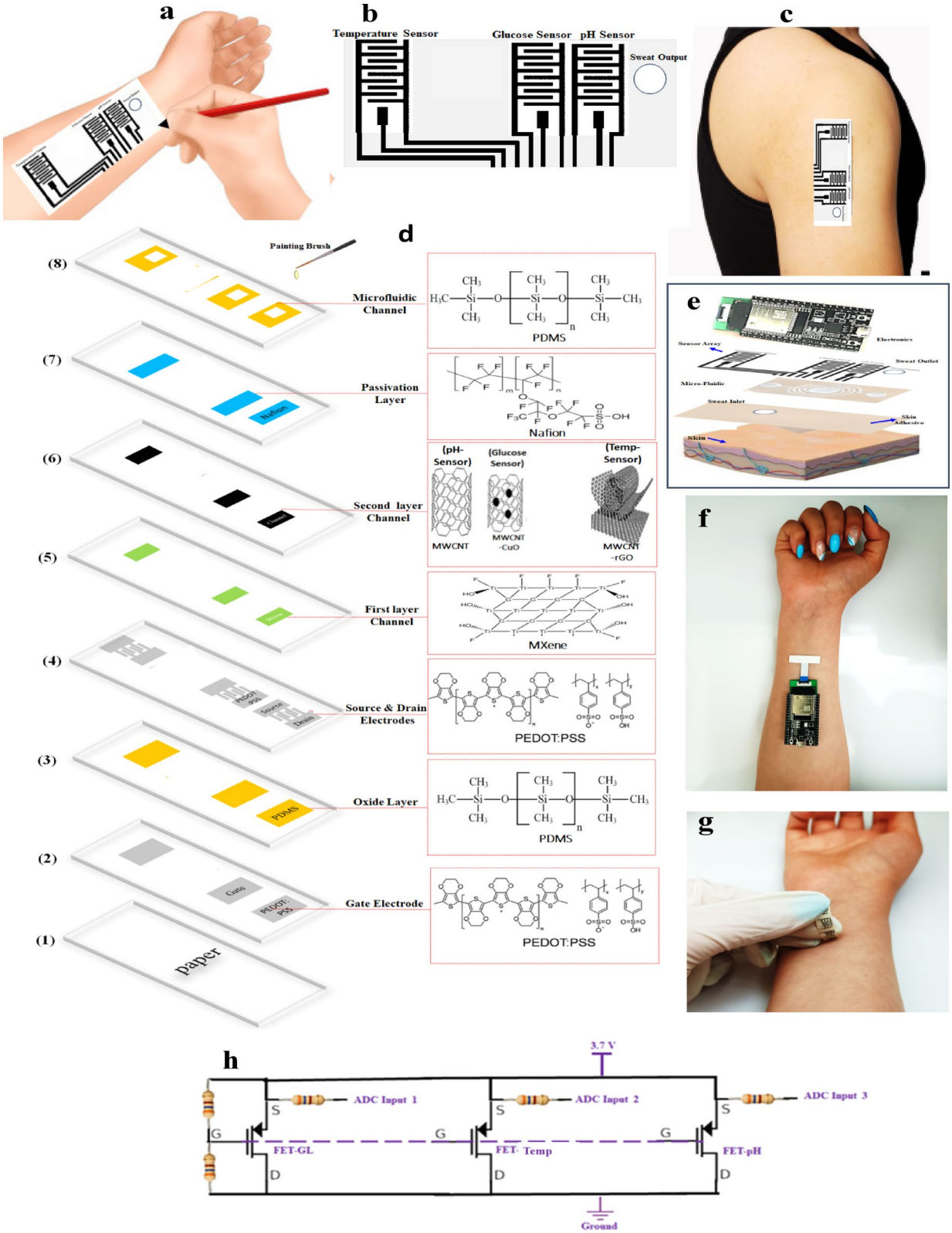

Fig. 2. (**a**,**b**) Illustration of the electronic skin, using ink-dipped paintbrush to draw on the paper, (**c**) wearable device seamlessly integrated with the skin. (**d**) Layers of the proposed FET biosensor. (**e**, **f**,**g**) Schematic of the proposed wearable FET biosensor, (**h**) Electrical circuit.

Preparation of CuO/MWCNT-COOH ink

To synthesize the CuO/MWCNT-COOH nanocomposite, 10 mg of CuO nanoparticles is combined with 50 mg of MWCNT-COOH using a precise balance. The resulting mixture was meticulously ground together in a mortar until a soft and consistent texture was achieved. Next, the MWCNT-COOH/CuO blend was carefully added to a vial containing 2 cc of deionized water. The solution was stirred by a magnetic stirrer while being heated on a hot-plate set at 60 °C for 2 h. During this time, a NaOH solution was gradually introduced drop by drop into the vial. Following the chemical reaction, the solution was transferred to a specialized centrifuge vial and centrifuged at 3800 rpm for 5 min. Subsequently, ultrasonication was employed for an additional 5 min to ensure thorough mixing and dispersion. This entire process was repeated thrice to guarantee the effective separation of impurities, resulting in a purified material ready for deposition.

Preparation of rGO/MWCNT ink

The process of dispersing 10 mg of reduced graphene oxide (rGO) and 100 mg of MWCNT in 10 mL of deionized water to create a homogeneous mixture involves several steps to ensure a uniform dispersion and optimal drawing performance. First, ultrasonication, by using high-frequency sound waves to create cavitation, breaks down any agglomerates or clusters of the rGO and MWCNTs, allowing them to disperse evenly throughout the water. Next, mechanical stirring was employed to further enhance the dispersion of the nanoparticles in the water, ensuring that the rGO and MWCNTs are evenly distributed and do not settle out of the solution over time. The combination of ultrasonication and mechanical stirring helps to achieve a stable ink formulation with good stability and optimal drawing performance.

Figure 3 shows the process of preparation and synthesis of (1) Ti_3C_2 MXene/MWCNT, (2) Ti_3C_2 MXene/CuO/MWCNT, and (3) Ti_3C_2 MXene/rGO/MWCNT.

Fabrication of bioelectronic FET sensors

The process involves drawing with electronic inks on paper. Firstly, the gate electrodes are meticulously drawn on a paper substrate using a painting brush dipped in ink of PEDOT: PSS. Then, a dielectric layer, typically an oxide layer composed of PDMS, is carefully applied to the substrate to isolate the gate electrode (in the back-gated structure). The source and drain interdigitated electrodes are then precisely drawn using PEDOT: PSS ink. The sensing area, known as the channel, is created using specific types of electronic inks tailored to different sensing applications. The Ti_3C_2 MXene/CuO/MWCNT composite was employed for glucose sensing. Ti_3C_2 MXene/MWCNT was used for pH sensing, and Ti_3C_2 MXene/rGO/MWCNT for temperature sensing. The materials have been utilized so that they can enhance the sensors' sensitivity to specific biomarkers. Graphene contacts pads, because of their high conductivity, are used for electrical connections to the readout circuit. To protect and cover the sensing channel, a layer of Nafion is applied. Nafion improves the sensor performance by enhancing selectivity, stability, and biocompatibility while preventing interference, facilitating ion exchange, and ensuring strong adhesion of sensing materials. A final layer of PDMS is added to create a microfluidic-like channel, enabling a controlled sample flow. The process is the same for the side gated FET, without drawing the oxide layer (see Figure S2 in the Supporting Information).

To ensure accurate and repeatable patterns are drawn on paper, some rules has been made that could successfully achieve accurate and repeatable patterns:

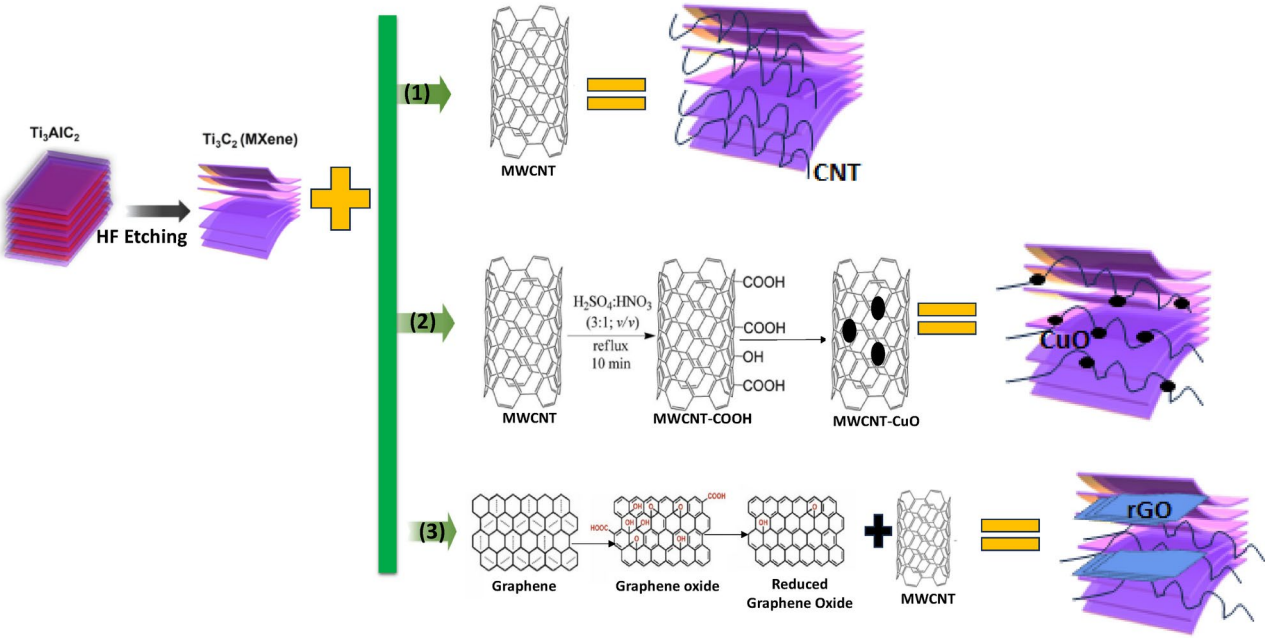

Fig. 3. Schematic process of preparation and synthesis of the channel materials.

1. First, a stencil has been employed and applied the ink through the open spaces onto the surface.
2. The ink quality and viscosity were adjusted so that it ensured the good adhesion and conductivity.
3. A steady paintbrush has been used to ensure precision. The same consistent brush strokes and movement speed has been used for all the structures.
4. The brush was not overloaded with ink and the amount of material applied is controlled to maintain consistency.
5. The first layer has been allowed to dry before applying the second layer.
6. Additionally, preliminary tests have been performed to refine our technique and improve the accuracy and all the above-mentioned conditions resulted in obtaining repeatable and accurate electrodes.

PCB design for wireless wearable device

The microcontroller unit utilized for real-time data collection, processing, and transmission to the host smartphone was an ESP32 equipped with built-in Wi-Fi capabilities. This PCB microcontroller was powered by a 3.7 V lithium rechargeable battery. Three ADC port of microcontroller were employed for sending glucose, pH, and temperature levels variation to smartphone. Additionally, a charge current with Type-C input was employed for charging rechargeable battery by mobile cable and solar cell. After one charge, the proposed wearable device can operate for 12 h. For connecting FET sensor array to microcontroller, a FPC FFC flat cable connector socket (12pin 0.5 mm) and a flat cable was used (see Figure S3 in the Supporting Information). A mobile application was employed for monitoring glucose, pH, and temperature sensors (see Figure S4 in the Supporting Information).

Electrical characteristics for 12 FETs

The schematic of the fabricated FET biosensors is shown in Fig. 4(A-D). Figure 4A and C, and Fig. 4B and D represent the back-gated and the side-gated FETs, respectively. In side-gated FETs, the gate electrode is positioned adjacent to the transistor channel on the same side. This side gate structure allows for easy access to the gate electrode for modulating the charge carrier density and the FET current (I_{ds}). In back-gated FETs, the gate electrode is located beneath the transistor channel, which allows for better control over the I_{ds} by adjusting the gate voltage. In this case the gate electrode is separated from the channel by an insulating layer.

Side-gated FETs are known for their high sensitivity to changes in the surrounding environment or analyte concentration due to the proximity of the gate electrode to the channel. Back-gated FETs can also exhibit high sensitivity, especially in bio-sensing applications, as the gate voltage applied to the back gate can effectively modulate the I_{ds} generated or increased due to exposure to the analyte concentration. Side-gated FETs may have lower transconductance compared to back-gated FETs, which can affect the amplification of the current signal in the sensor. Back-gated FETs often exhibit higher transconductance, which can be advantageous for amplifying the current signal and improving sensor sensitivity.

Initially, the electrical properties of the fabricated back and side gated FETs featuring a CNT channel were evaluated as standalone FETs without the presence of bioreceptors, as depicted in Fig. 4A(a, b) and Fig. 4B(a, b), respectively. The I_{ds} of the FET-based sensors exhibits a linear increase with V_{ds} ranging from 0 to 5 (V_{gs} = 0 to -3 V), indicating a good Ohmic behavior across a wide V_{ds} range. Beyond V_{ds}=5 V, the transistor operates in saturation, maintaining a constant I_{ds} with V_{ds} increment. The output characteristics (I_{ds}–V_{ds}) in Fig. 4A(a) and Fig. 4B(a) show a decrease in I_{ds} with positive gate voltages and an increase with more negative V_{gs} values, highlighting the significant gate control over the FET channel. Furthermore, the back-gated FET demonstrates the highest current amplification and the largest transconductance (g_m) compared to the side-gated FET. The calculated threshold voltage (V_t) of approximately 0 V have been obtained for both types of the FETs (Fig. 4A(b) and Fig. 4B(b)).

The combination of Ti_3C_2 MXene and MWCNTs as a channel material in FETs leverages the advantages of both materials. The hybrid structure benefits from the high conductivity of MWCNTs and the tunable properties of Ti_3C_2 MXenes, leading to improved charge transport and device performance. The synergistic effects of these materials can enhance the overall electrical characteristics of the FET including g_m, making it suitable for advanced electronic sensing applications When the Ti_3C_2 MXene/MWCNT structure is functionalized with -COOH groups (Ti_3C_2 MXene/MWCNT-COOH), the I_{ds} decreases compared with Ti_3C_2 MXene/MWCNT. This reduction in current can be attributed to the introduction of surface defects and charge trapping sites caused by the functionalization process. While the -COOH groups can enhance the hydrophilicity and facilitate further chemical modifications, they can also impede charge carrier mobility, leading to decreased current flow in the FET. By incorporating CuO into the Ti_3C_2 MXene/MWCNT channel, the g_m of the FET is enhanced. CuO serves as a p-type semiconductor that can improve hole mobility and increase the overall conductivity of the composite channel. The interaction between CuO and the Ti_3C_2 MXene/MWCNT matrix can create additional pathways for charge transport, leading to better device performance and higher current levels shown in Figs. 4C(a, b) for backgated FET, and Figs. 4D(a, b) for side gated FET. Adding rGO to the Ti_3C_2 MXene/MWCNT channel further enhances both the transconductance and the current. RGO because of its high conductivity and large surface area, can facilitate better charge transport. The combination of rGO with Ti_3C_2 MXene and MWCNTs can create a highly conductive network that improves the overall electrical properties of the channel. This synergistic effect results in enhanced performance metrics for the FET, making it suitable for high sensitivity applications and fast response times. Obtained results are shown in Figs. 4C(a, b) for backgated FETs, and Figs. 4D(a, b) for side gated FETs. In the proposed sensors, the use of the composite of MWCNTs and Ti_3C_2 MXene in FETs presents a promising avenue for developing advanced sensors. Careful design of the channel structure, including functionalization with -COOH, incorporation of CuO, and addition of rGO, allows for superior sensing properties, leading to improved performance in wearable applications.

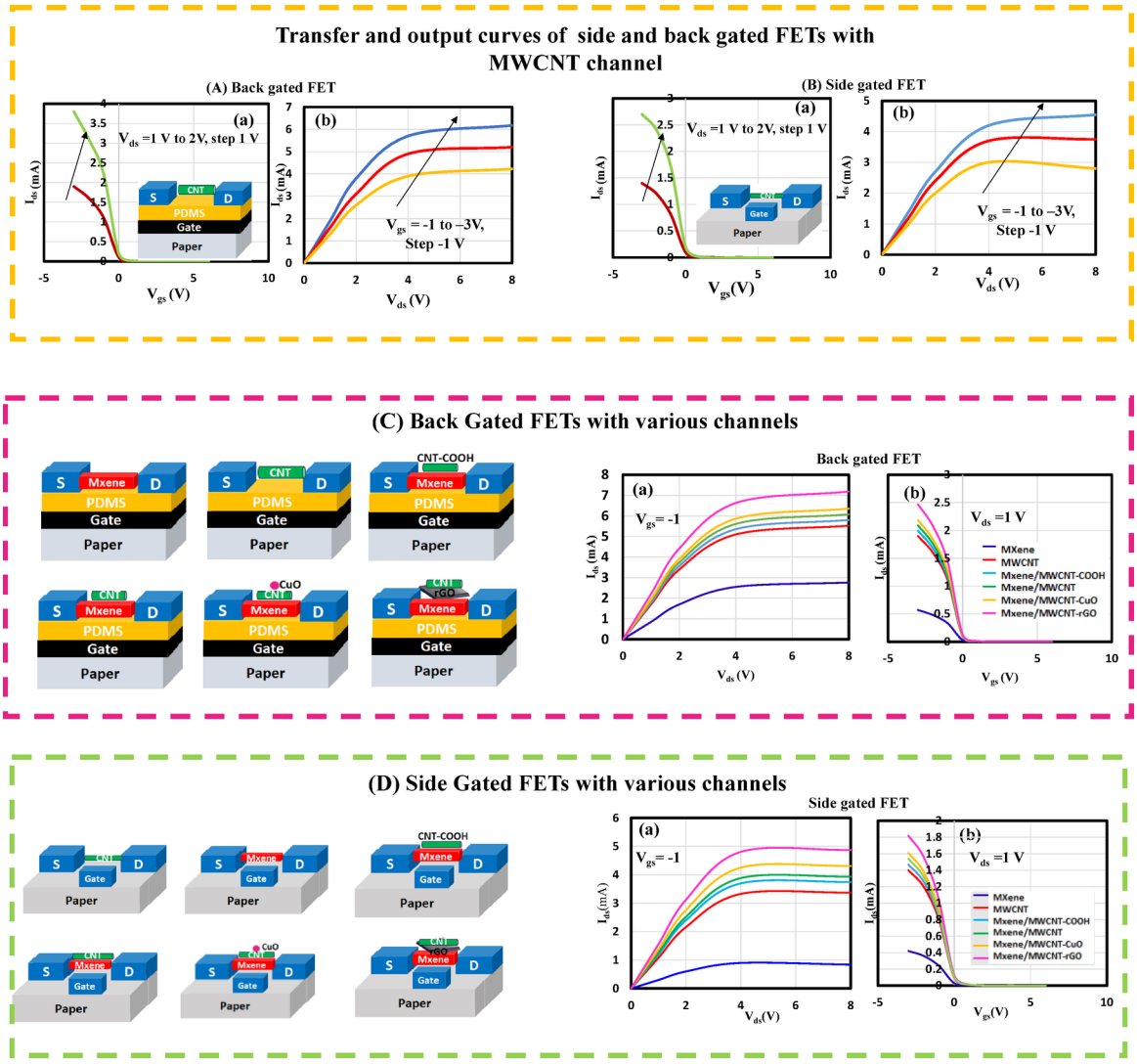

Fig. 4. The I-V curves for (Aa), (Ab) backgated FET with CNT. (Ba), (Bb) side gated FET with CNT, (Ca), (Cb) comparing the backgated FETs with various channels. (Da), (Db) comparing the side gated FETs with various channel.

Measurement results for 9 sensors

In this section, we present and analyze the response of the fabricated sensors. A total of 9 sensors have been fabricated to detect four parameters: glucose, pH, and body temperature. For each parameter, three types of sensors were designed: a resistive sensor (floated-gate FET), a side-gated FET, and a back-gated FET. The subsequent subsections will present and discuss each sensor individually including their three different gate designs.

Glucose-Sensor

Three designs for glucose detection by wearable paper-based FET sensors have been proposed. When the gate is float, the sensor structure is in fact a resistive Glucose-Sensor. The side gated FET Glucose-Sensor has its gate beside the channel and the back gate FET Glucose-Sensor has a back gate under the channel. The Ti_3C_2 MXene/CuO/MWCNT is the channel used for fabrication of Glucose-Sensors. In Fig. 5(Aa), the I_{ds} is plotted as a function of drain-source voltage (V_{ds}) in response to varying glucose concentrations. The graph illustrates that I_{ds} decrease for higher glucose concentrations. Subsequently, in Fig. 5(Aa), I_{ds} is plotted against glucose concentrations for different drain voltages (with V_{gs} held at -1 V). It is evident that with an increase in V_{ds} under constant gate voltage, both I_{ds} and sensor sensitivity (slope of I_{ds} vs. glucose concentration curve) rise. The effect of gate-source voltage (V_{gs}) on the back-gated and side-gated, and floated-gate FET biosensor's performance (effect of gate design) have been investigated in Fig. 5Ab. The V_{ds} was set as 1 V, and the I_{ds} was recorded when exposed to a specific glucose concentration (300 µM in this instance).

In Fig. 5(Ab), the I_{ds} vs. V_{gs} curves show a significant rise in I_{ds} in the back-gated FET Glucose-Sensor which is attributed to the modulation of charge carriers generated in the FET channel by the gate electric field, signifying

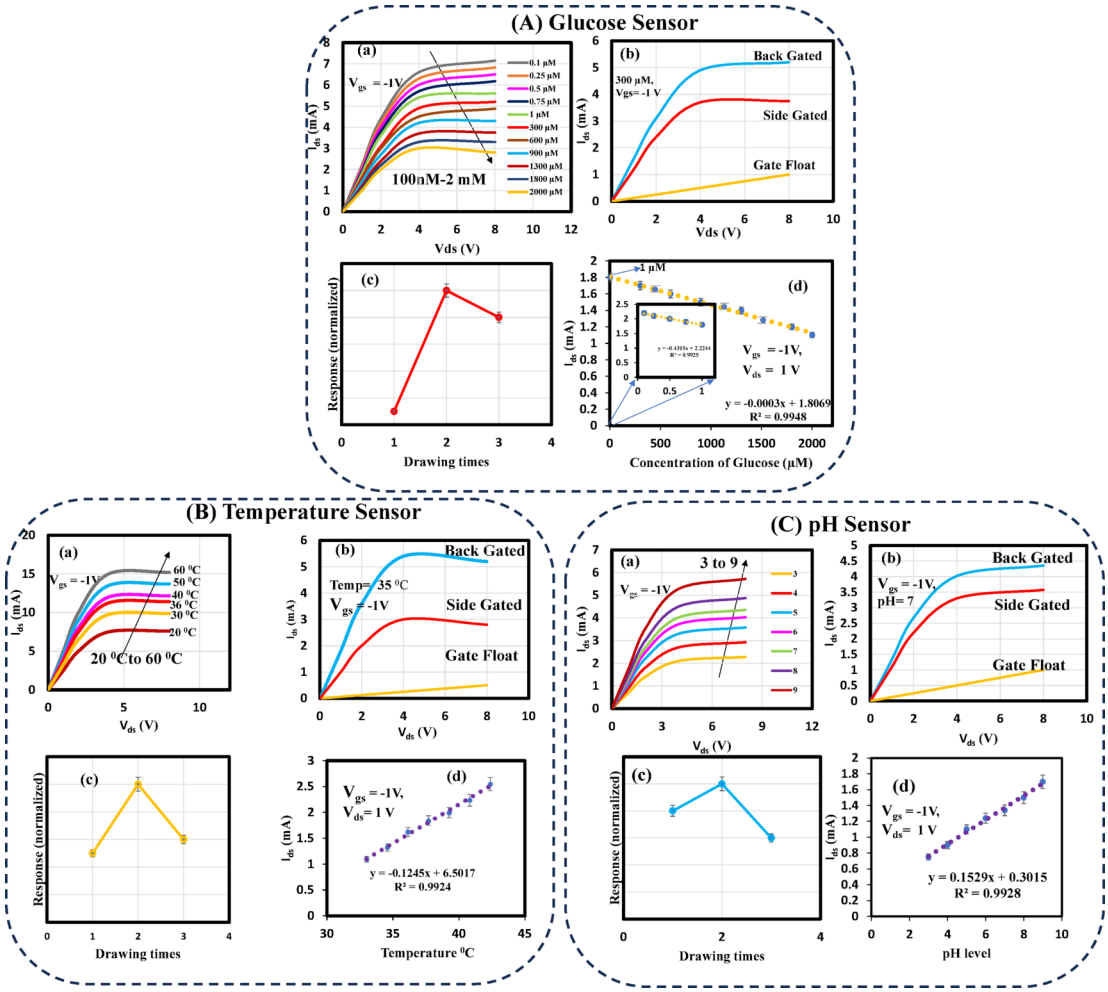

Fig. 5. Output characteristic curves for backgated (**A**) glucose, (**B**) pH, and (**C**) temperature-sensors.

an improved sensor reaction to glucose solutions. Figure 5(Ac) shows the effect of ink concentration (drawing times) on the sensor response. The proposed sensor shows the highest response in the two-time drawing. The thickness of the channel in the FET, as observed in AFM images, is 1000.07 nm for two passes of drawing. In the case of a single pass, the response is lower because some of the ink is absorbed by the paper. Conversely, for three passes, the sensor's response decreases compared to the two-pass drawing. This reduction is attributed to the increased thickness of the channel, which hinders the transfer of charge carriers, resulting in a decrease in g_m of the FET. The sensitivity of the FET improves with increasing V_{ds}, demonstrating a wide detection range of concentrations from 0 to 2 mM with high sensitivity. The sensor has a linear response with a LOD of 10 nM as shown in Fig. 5(Ad). Based on the obtained results, the back-gate FET glucose biosensor offers advantages such as higher sensitivity and lower LOD compared to the side-gate one. This superiority can be attributed to the back-gate sensor's enhanced current amplification due to its stronger and more uniformly distributed electric field, along with a lower potential drop between the channel and gate. The performance is enhanced by the side gate design compared to the resistive structure, with the back gate design yielding the highest response.

The operation of side-gated and back-gated FETs can be described using similar equations based on the principles of field-effect transistors. Here are the general formulas for the operation of theses FETs:

The channel current (I_{ds}) in a back and side-gated FET operating in the linear region can be described by the equation:

$$I_{ds} = \frac{1}{2}\mu_n C_{ox}\left(\frac{W}{L}\right)\left[2\left(V_{gs} - V_t\right)V_{ds} - {V_{ds}}^2\right] \quad (1)$$

The channel current (I_{ds}) of the FET in the saturation region is calculated by

$$I_{ds} = \frac{1}{2}\mu_n C_{ox}\left(\frac{W}{L}\right)\left(V_{gs} - V_t\right)^2 \quad (2)$$

The transconductance g_m of the FET is defined with the equation:

$$g_m = \frac{\partial I_{ds}}{\partial V_{gs}} \tag{3}$$

Where W is the channel width, μ_n is the electron mobility, C_{ox} is the oxide layer capacitance per unit area, V_{gs} is the gate-source voltage, V_t is the threshold voltage, V_{ds} is the drain-source voltage.

The sensor's sensing mechanism revolves around the chemical reactions and transistor action involved in the glucose sensing of proposed backgated FET. Initially, when glucose interacts with CuO a half-oxidation reaction transforms Cu(II) into Cu(III)[35]:

$$CuO + OH^- \rightarrow CuO(OH) + e- \tag{4}$$

Subsequently, a nonenzymatic oxidation-reduction reaction occurs between the formed Cu(III) oxyhydroxide and adsorbed glucose molecules, leading to the production of gluconolactone, which hydrolyzes into gluconic acid. This reaction results in the oxidation of glucose and the reduction of metal oxyhydroxide CuO(OH).

$$2CuO(OH) + \text{glucose} \rightarrow 2CuO + \text{gluconolactone} + H_2O \tag{5}$$

$$\text{Gluconolactone} \rightarrow \text{Gluconic Acid} \quad \text{(Hydrolysis)} \tag{6}$$

The presence of Ti_3C_2 MXene facilities adsorbed glucose molecules and MWCNT facilities transferring electrons to PEDOT: PSS electrodes by ballistic properties, generating a larger number of electrons and decreasing the conductivity of the p-type FET channel, thereby elevating the FET current. The gate amplifies this current, enabling the selective sensing of different concentrations of glucose effectively. As the glucose concentration rises, the number of electrons also increases and p-type FET current decreases.

In the side gated FETs, the electric field is applied through the solution by means of the metallic side-electrode which is considered as the gate electrode. In this design, Since the electrolyte is an ion conductive, the sensor performance becomes dependent to the changes of electrolyte caused by the analyte as well as the changes in the channel characteristics (see Figure S5 in the Supporting Information).

In the side gated FETs, also the reactions of (1),(2), and (3) take place[36]. During the oxidation of glucose, the electrons will be transferred to gate and the potential distribution in the gate electrode of side-gated FET changes according to the Nernst equation[37]:

$$V_{G2} = \frac{KT}{2q} Ln[ne^{-1}] + C \tag{7}$$

where T is the temperature, k is the Boltzmann constant; q is the electric charge, $[ne^{-1}]$ is the number of electrons released during oxidation and C is a constant value. As a result, the gate voltage applied on the channel can be obtained by the equation[37]:

$$V_{G1} = V_G - \frac{KT}{2q} Ln[ne^{-1}] - C \tag{8}$$

In the side gated FET, there are two potential differences across the channel and the gate (see Figure S5 in the Supporting Information) which means that there are two capacitances:

$$V_G = V_{G1} + V_{G2} \tag{9}$$

$$C_{ox} = C_{VG1} + C_{VG2} \tag{10}$$

and

$$Cox = \frac{q}{V_G} = \frac{k \varepsilon A}{D} \tag{11}$$

We can compare the capacitance of the oxide layer in a back-gated FET and side gated FET by distance between the capacitor surfaces:

$$C_{ox\ (side\ gated)} > C_{ox\ (back\ gated)} \tag{12}$$

As the distance between the capacitor surfaces in a back gated FET increases, the capacitance of the oxide layer ($C_{ox\ (back\ gated)}$) decreases at a constant gate voltage (V_g) according to Eq. 11. This reduction in capacitance leads to a decrease in the electrical charge induced in the capacitance, which in turn results in a lower electrical charge in the channel of a side gated FET. Consequently, the current through the FET decreases, leading to a reduction in the transconductance (g_m) of the device compared to a back gated FET (see Eqs. 1, 2, and 3). In a back-gate structure, electrons released during the oxidation of glucose are directly transferred to the electrodes through the channel of the back gated FET. The larger capacitance of the oxide layer in this configuration (see Eq. 12) allows V_g to induce a greater electrical charge in the channel compared to a standard side-gated structure. Therefore, V_g in back-gated FET can enhance the oxidation of glucose and facilitate the transfer of more charge carriers to the channel, ultimately increasing the device's sensitivity to glucose.

Temperature-sensor

Since the variations in temperature during glucose detection can result in inaccurate readings, it is crucial to integrate temperature sensors for calibration to account for this effect. By utilizing the Ti_3C_2 MXene/rGO/MWCNT temperature sensor near the FET sensors, it is possible to precisely detect the temperature changes in the area (see Figure S4 in the Supporting Information). The linear relationship between the measured relative resistance changes and temperature within the physiologically relevant range of 20 to 60 °C yields a sensitivity of −11.2. For comparison, FET temperature-sensors with resistive, side-gated, and back-gated FET designs are proposed. The fabrication process involves using Ti_3C_2 MXene/rGO/MWCNT as the channel material. Figure 5Ba shows an increase in I_{ds} at elevated temperatures. Raising the V_{ds} while keeping a constant V_{gs} results in increased I_{ds} and improved sensor sensitivity to temperature changes. The sensitivity of the FET improves with higher V_{ds}, with a detection range from 20^0C to 60^0C with high sensitivity. Figure 5(Bb), shows that the back-gated FET, provides higher response to the temperature than other structures. The fabricated temperature sensos were calibrated with a commercial temperature sensor (LMT70EVM).

The effect of gate electrode design on the performance of the FET biosensors was studied with V_{ds} set at 1 V, and I_{ds} recorded at a specific temperature (35 ^{0}C) in Fig. 5Cb. The back-gate biosensor offers higher output and larger sensitivity. Figure 5(Bc) demonstrates the impact of ink concentration, showing the highest sensor response with two drawing cycles. The thickness of the channel in the FET, as observed in AFM images is 2700 nm for two passes of drawing. The same mechanism for two drawing occurs for Temp sensors (see explanation of glucose sensor in Sect. 7.1). The sensor exhibits a linear response as depicted in Fig. 5(Bd).

The electrical conductivity of rGO is sensitive to temperature changes[38]. As the temperature increases, the intrinsic carrier concentration and mobility of charge carriers (electrons and holes) in rGO generally increase, leading to a decrease in electrical resistivity. The temperature dependence of conductivity can often be described by an Arrhenius-type equation, where the conductivity (σ) is related to temperature (T):

$$\sigma\,(\mathrm{T}) = \sigma e^{-\frac{\mathrm{Eak}}{\mathrm{T}}} \tag{13}$$

Where:

- σ is a pre-exponential factor,
- Ea is the activation energy for conductivity,
- k is Boltzmann's constant,
- T is the absolute temperature.

The synergy of these materials (Ti_3C_2 MXene/rGO/MWCNT) enhance sensitivity and provides a more linear response to temperature changes, making them suitable for precise measurements. The unique thermal and electrical properties of the composite allow for quick responses to temperature changes. The combined materials can be processed into flexible structures, making them adaptable for various applications, including wearable sensors. The same sensing mechanism works for side and back gated FETs in temperature sensing (see Eqs. 1–3, and 7–12).

PH-Sensor

The Ti_3C_2 MXene/MWCNT is utilized as the channel in the construction of wearable paper-based pH-Sensors. In Fig. 5(Ca), I_{ds} is depicted against the V_{ds} for various pH levels. It shows an increase in I_{ds} for higher pH concentrations. In Fig. 5(Ca), I_{ds} is plotted against pH levels for different drain voltages (with V_{gs} maintained at -1 V). It is evident that increasing V_{ds} under a constant gate voltage result in higher Id_s and sensor sensitivity (slope of I_{ds} vs. pH levels curve). The FET sensitivity enhances with rising V_{ds}, showcasing a broad detection range from 3 to 9 with high sensitivity. The influence of gate structure (back-gate, side-gate, and float-gate) on the biosensor performance was analyzed with V_{ds} set at 1 V, and I_{ds} recorded at a specific pH concentration (pH = 7). The I_{ds}-V_{gs} curve in Fig. 5(Cb) indicate an enhanced sensor response to pH solution by the back-gated FET. Figure 5Cc demonstrates the impact of ink concentration on paper, showing the sensor's highest response with two drawing cycles. The thickness of the channel in the FET, as observed in AFM images is 973 nm for two passes of drawing. The same mechanism for two drawing occurs for pH sensors (see explanation of glucose sensor in Sect. 7.1). The sensor exhibits a linear response as depicted in Fig. 5(Cd).

The Ti_3C_2 MXene sheets themselves are pH-responsive due to their hydroxyl surface groups, and this effect may be amplified with the choice of appropriate MWCNTs[39]. The change in proton concentration (H^+ ions) leads to a corresponding change in the surface charge density on the MWCNTs, which can be monitored through current changes measurements. However, pH sensing does not typically correspond to a single "reaction" like oxidation or reduction, but rather involves changes in the surface charge and conductivity of the MWCNTs as they interact with protons (H^+). For pH sensing the FET bias voltage was applied at 0.5 V to prevent the oxidation of glucose. Also, there is no any material on the surface of the pure MWCNTs for oxidation of glucose. This means that the MWCNTs only sense pH variations selectively. The influence of H^+ ions on the electronic properties of the p-type MWCNTs, leading to changes in the conductivity that can be monitored to infer pH levels is expressed as:

$$\sigma = f\left(\mathrm{H}^+\right) \tag{14}$$

Where:

- σ is the conductivity of the Ti_3C_2 MXene/MWCNTs,

- $f(H^+)$ signifies that conductivity is a function of the concentration of H^+ ions in the solution.

The sensing mechanism of both side-gated and back-gated Ti_3C_2 MXene/MWCNTs FET-based sensors can be explained in detail as follows. The direct interaction between semiconductor MWCNTs and H^+ ions, such as charge transfer, can significantly affect the conductivity of the Ti_3C_2 MXene and charge transfer to PEDOT: PSS electrodes. Additionally, the local screening of the electric field occurs due to the accumulation of ions at the interface between the MWCNTs and the solution. During operation, biasing the gate and the source-drain generates a current flow through the channel. The adsorption or interaction of H_3O^+ is then translated into a change in the source-drain current. To ensure the sensing process is reversible, an opposite polarity bias can be applied to the gate (V_{gs}<0), facilitating the desorption of weakly bonded ions.

The measurement results for the 9 sensors show that the back gated FET provides the highest output signal amplification through the electric field induced by the back gate voltage which allows for increased transport of charge carriers across the channel. This gate structure boosts the current, increases the transconductance (g_m), enhances the sensitivity, and reduces the LOD compared to side gated FETs. Additionally, the stronger electric field in the back-gate bioelectronic FET, with a lower potential drop between the channel and gate, facilitates electronic charge transport, resulting in a faster response time compared to electrochemical FETs. In the back-gate FET, a uniform electric field is applied to the channel via the oxide layer whereas in side gated structures (electrochemical FETs), it is applied through the electrolyte solution to the channel, allowing other molecules in the electrolyte solution to affect the electric field.

Material characterization

Figures 6(a, b) show the SEM images of the rGO when employed as the channel of FET sensor. The rGO structure, shows a fascinating sheet-like morphology characterized by a distinctive wrinkled and layered appearance. The jagged or irregular edges observed offer valuable visual cues regarding the reduction process undergone by the graphene oxide (GO) and the presence of functional groups, which play a significant role in influencing the sensor's performance and sensitivity toward the target analytes (see elemental mapping in FigureS6(d) in the Supporting Information).

In Figs. 6(c, d), the SEM images reveal the electrical connections of biosensors (the drawn electrodes using graphene). The layered configuration of graphene sheets creates a porous and interconnected structure essential for establishing excellent electrical contact in wearable applications (see elemental mapping in Figure S6(d) in the Supporting Information).

The FESEM images of MWCNTs in Figs. 6(e, f) confirm their unique tubular morphology and high aspect ratio. The images show the high density of the MWCNTs in the channel, with many of them interconnected to each other (see elemental mapping in Figure S6(a) in the Supporting Information). The tangled network of MWCNTs demonstrates their nanoscale dimensions, high surface to volume ratio, and that the material is capable of being flexible when subjected to mechanical bending which are suitable parameters for wearable paper-based FET sensors.

The FESEM images of MWCNT-COOH in Figs. 6(g, h) reveal their surface characteristics and increased diameter compared to pristine CNTs, confirming the chemical modification process (see elemental mapping in Figure S6(b) in the Supporting Information). The rougher surface and larger diameter observed in the images visually demonstrate the successful functionalization with carboxyl groups, enabling improved interactions with target molecules and enhancing performance in bio-sensing applications.

Figures 6(i, j) show SEM images of PEDOT: PSS, revealing a textured surface with a granular appearance that highlights its intricate structure. The interconnected polymer network seen in the images forms a conductive and uniform layer crucial for electronic devices and sensors. The roughness observed emphasizes the film-forming properties and conductivity of PEDOT: PSS, showcasing its potential for source, drain, and gate electrodes as a reliable conductive layer.

The FESEM and TEM images of MWCNT-CuO composites in Figs. 6 (k, l) show the hybrid structure formed by combining MWCNTs and CuO nanoparticles. The intricate morphology of the composite highlights the role of MWCNTs as a scaffold for CuO particles, enhancing properties for biosensing applications (see elemental mapping in Figure S6(c) in the Supporting Information). The attachment of CuO nanoparticles to MWCNT surfaces, as seen in the TEM image, enhances material sensing properties and provides selectivity for detecting glucose molecules.

The SEM image of Ti_3C_2 MXene reveals the layered structure of two-dimensional materials, showcasing a network of densely packed nanosheets as shown in Fig. 6 (m-p). The contrast observed in the SEM image shown in Figs. 6 (m-o) underscore differences in thicknesses; darker regions may indicate thicker aggregates or clusters, while lighter areas reveal single or few-layer nanosheets. The surface topography displays irregularities and defects, indicative of cleavage during the selective etching process used for Ti_3C_2 MXene synthesis. Also, high-resolution TEM imaging captured the morphology of Ti_3C_2 MXenes, where individual flakes exhibit a triangular shape as shown in TEM image in Fig. 6 (p).

The FESEM images of Ti_3C_2 MXene/MWCNT, Ti_3C_2 MXene/MWCNT-COOH, Ti_3C_2 MXene/CuO/MWCNT, and Ti_3C_2 MXene/rGO/MWCNT were utilized as channels of FET sensors, are shown in in Figs. 6 (q-t). The MWCNTs are distributed on the surface of Ti_3C_2 MXenes. The MWCNTs and rGO are marked in the FESEM images.

The XRD characterization pattern displayed in Fig. 7a illustrates the MWCNT, rGO, MWCNT-COOH, rGO/MWCNT, CuO/MWCNT, Ti_3C_2Mxene and PEDOT: PSS. XRD without the presence of any impurity. As for the XRD pattern of MWCNT, a peak at $2\theta = 25.1°$ is typically associated with the (002) reflection plane of the MWCNTs, indicating the nanotube structure and, a peak at $2\theta = 42°$ corresponds to the (100) reflection plane of the MWCNTs, reflecting the hexagonal lattice arrangement of carbon atoms along the nanotube axis. The XRD

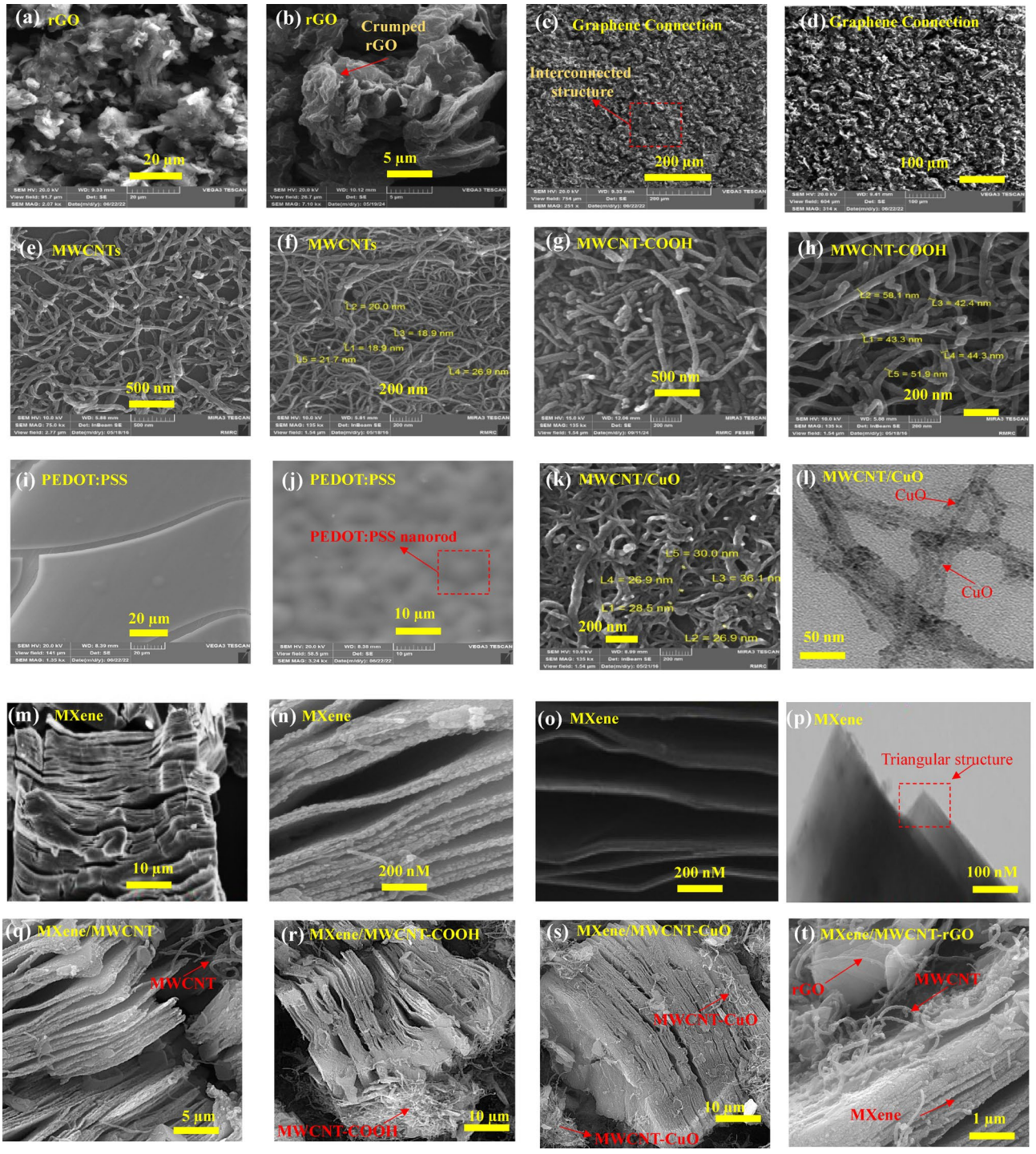

Fig. 6. The SEM, FESEM, and TEM images of the FET channel materials.

pattern of rGO shows two peaks: one small peak centered at $2\theta = 11.1°$(attributed to the 002 plane) and a broad peak at $2\theta = 25°$ (attributed to the 002 plane), corresponding to an interlayer distance of 4.46 and 3.52 Å (the interplanar spacing of crystal lattice planes), respectively. The acid-functionalized MWCNT exhibits distinctive broad peaks at $2\theta = 26.2°$ and $2\theta = 44°$, which, upon reaction with rGO and subsequent reduction, shift slightly towards lower 2θ values. For MWCNT/rGO ($2\theta = 24.7°$), indicating interaction between carbon nanotubes and graphene. Considering the XRD pattern of CuO/MWCNT, the peak at $2\theta = 25.1°$ is related to MWCNT (attributed to the 002 plane), and the peaks at $2\theta = 24.1°$, 31.1° are related to CuO nanoparticles (attributed to the 111 and 202 planes, respectively), showing successful formation of CuO/MWCNT. The XRD patterns for Ti_3C_2 MXene display distinct peaks at 9.1°, 18°, 26°, and 60°, which correspond to the (002), (006), (008), and (110) crystal planes, respectively. The absence of the aluminum peak around 38° indicates the effective removal of the

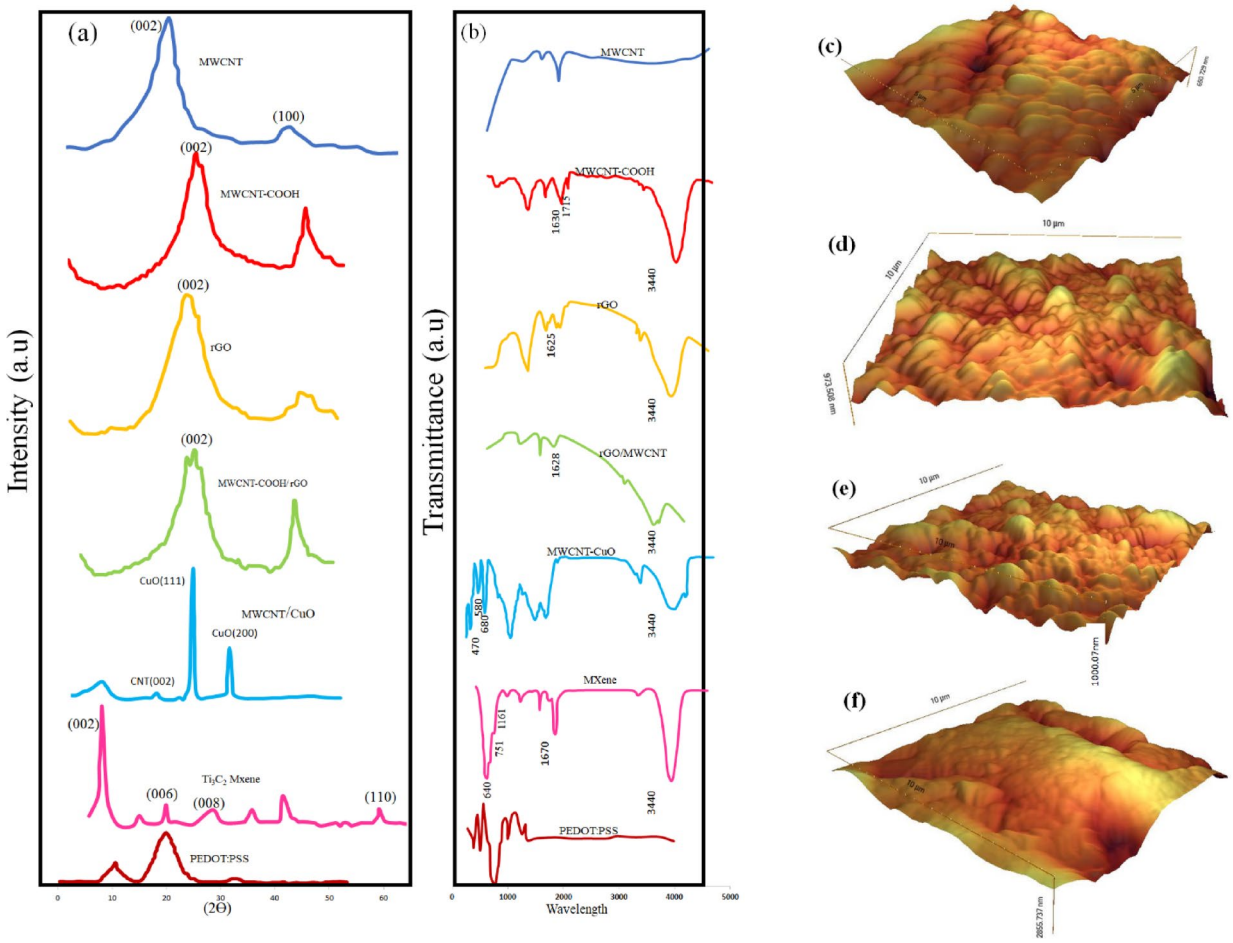

Fig. 7. (**a**) XRD, (**b**) FTIR, and AFM images of FET channel materials (**c**) MXene/MWCNT, (**d**) MXene/MWCNT-COOH, (**e**) MXene/ CuO/MWCNT, and (**f**) MXene/rGO/MWCNT.

aluminum layer from the MAX precursor. Additionally, peaks appearing at 42° is attributed to TiC, which is an impurity present in the MAX phase precursors. The XRD pattern of PEDOT: PSS, has a peak at $2\theta = 12.5°$ which is attributed to the interchain spacing in the PEDOT: PSS. It indicates the arrangement of the polymer chains within the material. A peak at $2\theta = 23°$ is typically attributed to the Bragg reflection from the PSS chains in the PEDOT: PSS complex. It reflects the ordering or alignment of the PSS chains within the material.

Figure 7b displays the FTIR spectra of the sensors' sensitive materials. The rGO exhibits characteristic peaks that correspond to oxygen functional groups such as C = O, C–OH, and C–O–C at 1715, 1030, and 1200 cm^{-1}, respectively. Peaks at 3440 and 1390 cm^{-1} indicate the presence of hydroxyl (–OH) groups, while the broad spectrum ranging from 2500 to 3500 cm^{-1} is attributed to carboxylic (–COOH) groups. Acid functionalization of MWCNT introduces –COOH groups (1715 cm^{-1}) and –OH groups (3440 cm^{-1}). The reaction between MWCNT-COOH and rGO, followed by reduction with hydrazine hydrate, produced the MWCNT/rGO, which exhibits a hump (indicative of the –COO linkage) adjacent to the C = C stretching at 1628 cm^{-1}, confirming the chemical bonding between MWCNT and graphene. In FTIR pattern of CuO/MWCNT, the absorption peaks at 470 cm^{-1} and 580 cm^{-1}, and 680 cm^{-1} are assigned to the Cu–O bonds and confirm the decoration of CuO on MWCNT. The FTIR spectrum of Ti_3C_2 MXene showed a distinct peak at 3440 cm^{-1}, which was attributed to the hydroxyl (–OH) group. An additional peak at 1670 cm^{-1} further validated the presence of a hydroxyl group and indicated hydrogen bonding with water molecules. Peaks observed at 1161 cm^{-1}, 751 cm^{-1}, and 640 cm^{-1} were associated with Ti–F, Ti–O, and Ti–C bonding, respectively. The peak at 1040 cm^{-1} in the FTIR pattern of PEDOT: PSS, is attributed to the C-S stretching vibration in the PSS component of the blend. It indicates the presence of sulfonate groups in PSS. Peak at 1255 is associated with the stretching vibration of the C-O-C ether linkage in the ethylenedioxythiophene (EDOT) unit of PEDOT. It is a characteristic peak of the PEDOT component.

The AFM images of the proposed four channel materials in Fig. 7(c-f) are used to visualize their surface morphology and roughness. Figure 7c, for Ti_3C_2 MXene/MWCNTs, the prominent peaks and valleys highlight the unique arrangement and dimensions of the nanotubes. This reflects the alignment and dispersion of MWCNTs, providing insights into their surface roughness and potential aggregation. Figure 7d, for Ti_3C_2 MXene/MWCNT-COOH, illustrates the effect of carboxyl functional groups on the surface of MWCNTs which enhances interfacial adhesion to other materials. MWCNT-COOH demonstrates increased surface complexity,

as the carboxyl groups contribute to a more heterogeneous surface with greater roughness compared to pristine MWCNTs. The composition of MWCNT-COOH with CuO results in an increase in topographical height (Fig. 7e). Also, the integration of rGO sheets with Ti_3C_2 MXene/MWCNT creates a layered structure, revealing that the rGO layers appear as flat, sheet-like structures (Fig. 7f).

Selectivity, stability, repeatability, and reproducibility

The repeatability of the glucose, temperature, and pH sensors was tested and respective RSDs of 0.2%,0.15%, and 0.21% were obtained which demonstrates a high measurement repeatability of the sensors (Fig. 8(a-c). For stability test, after a 17-days period, a slight decrease of 1.5%, 1.8%, 2.1% were observed in glucose, temperature, and pH sensors responses, respectively, indicating a high stability and reliability. Attaining reproducibility values of 0.11%, 0.13%, and 0.18% for the sensors, highlights a high level of reproducibility of the fabrication process (Fig. 8(a-c). Additionally, as shown in Fig. 8d, the I_{ds}-V_{gs} graphs for four repeated measurements at 0.5 µM glucose are nearly identical, confirming the sensor's reliability in delivering consistent output. This demonstrates the excellent repeatability of the fabricated biosensor. By testing the sensor's response to common interfering species such as ascorbic acid, sodium chloride (5mM), uric-acid (1mM), lactose (10mM), fructose (10 mM), and dopamine (500µM), the high selectivity of the proposed glucose biosensors was demonstrated (Fig. 8e). The results indicated the respective 1.5% decrease in the glucose responses confirming the sensor's ability to

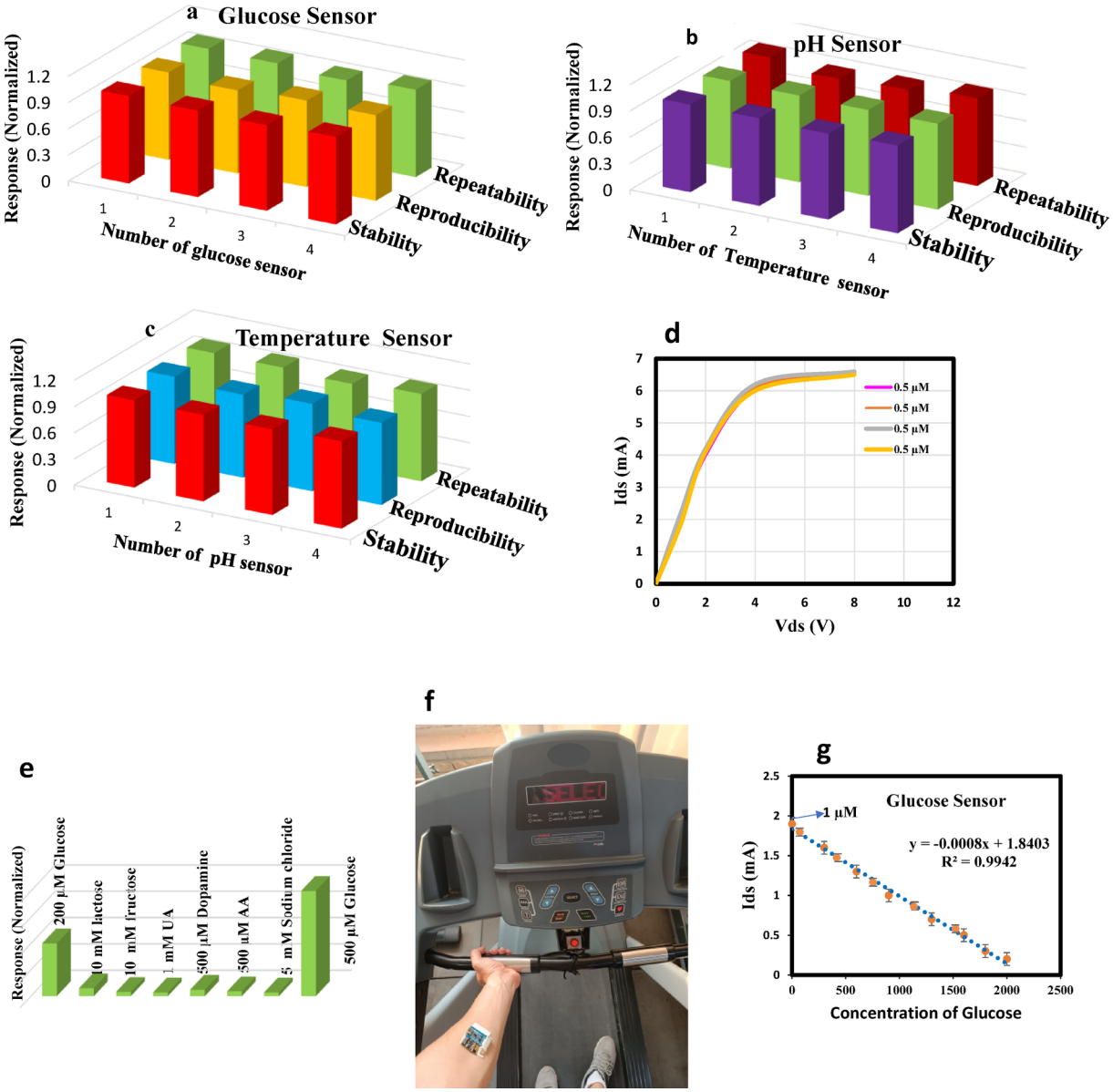

Fig. 8. Reputability, reproducibility, and stability tests for (**a**) glucose sensor, (**b**) pH-Sensor, and (**c**) Temperature sensor. (**d**) V_{gs}-I_{ds} graphs for four repeated measurements towards 0.5 µM glucose (**e**) Selectivity test for (**f**) Glucose. (**g**) Image of a volunteer post-exercise.

accurately detect the target analytes amidst potential interference. Selectivity was tested with four repetitions, resulting in an RSD of 0.02%. This results further confirms that the glucose sensor selectively detects the glucose through its oxidation at the surface of the Ti_3C_2 MXene/CuO/MWCNT ternary composite, which is related to the redox reactions of Cu^{2+} and Cu^{3+} ions. The pH sensor specifically interacts with H^+ ions, displaying no reactivity with glucose due to the lack of oxidation processes at the surface of pure MWCNTs in the MWCNT/Ti_3C_2 MXene composite. The results of this paper shows that MXene enhances the device performance because of its characteristics like large surface area, functional groups, improving charge transport, responding to H^+ ion concentration changes, enhancing catalytic properties, and stability in aqueous environments.

Calibration of glucose biosensors based on temperature and pH variations

At this stage the proposed glucose sensor has been calibrated based on the simultaneously measured temperature and pH. The calibration process begins with assessing the sensor's responses as a function of these variables. The FET current corresponding to a specific glucose concentration increases with rising temperature and pH levels (Figure S10). The influence of temperature and pH on the response of the sensor to glucose concentration, can be compensated by using compensation factors S_t and I_t for temperature, and correspondingly, S_p and I_p for pH. The calibrated glucose concentration is then calculated using the corrected slope and intercept from the linear fit (for further details, refer to Supporting Information Sect. 5.1 and 5.2.

On-body evaluation of the calibrated FET sensors integrated with a wireless patch

The integration of a calibrated glucose sensor with a Wi-Fi microcontroller allows for on-body sampling of sweat and subsequent glucose, pH, and temperature analysis through smartphone (Fig. 8f). To ensure safety and reliability in on-body measurements, the sensor's performance is evaluated in near-neutral solutions, such as artificial sweat, which closely resembles the chemical composition of human perspiration. Prior to on-body testing, the sensor is calibrated using artificial sweat at varying glucose concentrations (see the linear fitting curve in Fig. 8g). The accuracy of glucose concentration measurements in sweat—taken before, immediately after, and two hours after a meal—is confirmed by comparison with readings from a commercial glucometer (see Figure S7 in the Supporting Information).

Utilizing a skin adhesive medical tape, the wearable sensor is securely attached to the skin and remained stable even during mechanical bending. The obtained results of flexibility tests of the wearable sensor show that there is no satisficing change under mechanical deformation (see Figure S8 in the Supporting Information). The sensor array continually collects sweat samples for dynamic analysis of glucose levels before, immediately after, and two hours after a meal (see Figure S9 in the Supporting Information). Since sweat pH and body temperature can vary due to human activities, such as vigorous exercise or digestive enzyme activity after a meal, both sweat pH and skin temperature are measured simultaneously (see Figure S11a in the Supporting Information). Consequently, glucose levels measurements can be calibrated using adjusted slopes and initial values of I_{ds} derived from a linear fit based on the measured temperature and pH, enabling precise assessment of glucose concentrations on the body (see Figure S11b in the Supporting Information). This real-time calibration ensures a more accurate reflection of real blood glucose levels, especially the increase observed following the meals.

Recent advancements in wearable sensors are summarized in Tables 1 and 2, and 3. Table 1 shows that the proposed glucose sensor boasts a wide detection range, an extended lifespan, a low LOD, and an enhanced sensitivity. Table 2 demonstrates that the proposed temperature sensor offers high sensitivity and rapid response time. Finally, Table 3 reveals that the proposed pH sensor exhibits the highest sensitivity among the sensors reviewed. As shown in this article, our proposed FET sensors exhibit a rare capability with current outputs in the milliampere (mA) range, in contrast to the microampere (μA) range typically reported in other works, highlighting the superior performance of our technology. This distinction is crucial for achieving enhanced sensitivity, reduced noise, and improved accuracy. Furthermore, after calibrating for temperature and pH, our device achieves an accurate glucose measurement in sweat, providing true glucose levels without dependence on pH or temperature fluctuations, underscoring its significant advantage in detecting biomarkers in sweat.

Material	Recognition Molecule	Method	Sensitivity μA mM^{-1}	DR mM	LOD (μM)	Rt (s)	Lt Day	Ref
Au-ZnO	GOx	Electrochemistry	-	0.047–0.305	5.5	-	0.17	[40]
MXene/Pt	Free-Enzymatic	Electrochemistry	3.43	0–8	-	-	-	[6]
Au/Graphene	GOx	Electrochemistry	-	0–5	0.1	-	14	[41]
Au	GOx -chitosan	Electrochemistry	0.002	0-0.3	-	-	14	[42]
XSBR PEDOT: PSS-MWCNTs/AuNPs	Free-Enzymatic	Electrochemistry	-	0.050–0.6	3.2	-	-	[43]
PBNPs/MWCNT-COOH	GOx	Electrochemistry	11.87	0–1	7	-	-	[44]
PB-PEDOT NC	Free-Enzymatic	Chronoamperometry	-	0.00625- 0.8	6.25	-	-	[45]
PEDOT: PSS/ MXene /CuO//MWCNT	Free-Enzymatic	FET	1750	0.001-2	0.01	1	17	Our work

Table 1. Wearable sweat glucose sensors recently reported. DR: Detection range, LOD: limit of detection, Rt: response time, Lt: life time, PB: prussian blue, poly(3,4-ethylenedioxythiophene: PEDOTNC, NPs: nanoparticles, XBR: carboxylated styrene butadiene rubbe.

Material	DR (°C)	TCR (%/°C)	Rt	Advantage	Substrate	Ref
Ag/PEDOT: PSS	25–45	0.094, and − 1.39	-	Disposable, multi modal.	Glossy paper	46
Ag ink	25–45	0.234	-	-	Fabric	47
CNT/polyaniline nanofibers	15–45	−1	1.8 s	Flexible, stretchable, durable, no hysteresis, sensor array	PET	48
CNT/PEDOT: PSS	20–80	−0.25	∼1–2 s	Flexible, sensor array, multi modal sensing (strain-temperature)	Polyester	49
Hydrojel (Liquid metal, sodium alginate, and poly acrylic acid)	0–60	6.7	-	-	Flexible	50
Graphene/PDMS	35–45	21.4	1.6 s	Flexible, stretchable, biocompatible	Flexible	51
PEDOT: PSS/rGO/PDMS	30–50	-1.69	-	Flexible, stretchable, multi modal sensing (strain, temperature)	PET	52
Ag	20–60	22	-	-	Kapton	53
PEDOT: PSS/MXene/rGO /MWCNT	20–60	-11.42	0.9 s	Flexible, bendable, low cost, sensor array, disposable, biocompatible	Paper	Our work

Table 2. Wearable temperature sensors recently reported.

Material	Sensing mechanism	Substrate	Sensitivity ($mV\ pH^{-1}$)	DR (pH)	Rt	Ref
Graphite	Potentiometric	Cellulose-polyester blend	4	6–9	-	54
Iridium Oxide	Potentiometric	Ripstop silver	17.15	4–8	-	55
PEDOT: BTB	Chemo-resistive	Bio-ceramic fabric	7.5	2.2–7.8	-	56
CNT/Polyaniline	Potentiometric	Waterproof polyester	45.9	5–9	-	57
ZnO	FET	polysilicon	-59	1–9	-	58
H_xWO_3	Potentiometric	PET	-53.6	2–8	10.5 s	59
PANI	Potentiometric	PEN	-56.2	4–8	-	60
PEDOT: PSS/ MXene/MWCNT	FET	Paper	283.3	3–9	1s	Our work

Table 3. Wearable sweat pH sensors recently reported.

The results shows that the development of the proposed wearable bioelectronic FET biosensors drawn on paper for continuous monitoring of sweat combined with wireless electronics modules represents a promising, invasive, and cost-effective approach for managing, controlling, and diagnosing related diseases at early stages.

Conclusion

The study introduced Organic Bio-FETs drawable on paper as wearable non-invasive devices for sensing essential biomarkers such as glucose. Drawable glucose, pH, and temperature-sensors were proposed as innovative Bio-FET devices offering a versatile and cost-effective solution for real-time health monitoring, capitalizing on the unique properties of paper substrates and the sensitive detection capabilities of FET technology. The results showed that the back-gated structure exhibited more sensitive performance than the side gate one. The proposed glucose sensor could provide high sensitivity and low LOD. All the fabricated sensors showed high sensitivity and promising reproducibility, stability, and repeatability, which makes them suitable for wearable health monitoring applications. The proposed glucose sensor has been calibrated based on the simultaneously measured temperature and pH. The glucose, pH, and Temperature sensors integrated in a single device combined with IoT-based wireless data transfer capability presented a comprehensive solution for continuous health monitoring.

Data availability

The datasets used and/or analyzed during the current study available from the corresponding author on reasonable request.

Received: 5 January 2025; Accepted: 29 April 2025
Published online: 09 May 2025

References

1. Zhang, S. et al. On-skin ultrathin and stretchable multifunctional sensor for smart healthcare wearables. *Npj Flex. Electron.* **6**, 11 (2022).
2. Mao, P., Li, H. & Yu, Z. A. Review of Skin-Wearable sensors for Non-Invasive health monitoring applications. *Sensors* **23**, 3673 (2023).
3. Monfared Dehbali, M., Farahmandpour, M., Hamedi, S. & Kordrostami, Z. Development of a portable smart glucometer with two electrode bio-electronic test strip patch based on Cu/Au/rGO/PEDOT: PSS. *Sci. Rep.* **13**, 9505 (2023).
4. Farahmandpour, M., Kordrostami, Z., Rajabzadeh, M. & Khalifeh, R. Flexible bio-electronic hybrid metal-oxide channel FET as a glucose sensor. *IEEE Trans. Nanobiosci.* (2023).

5. Kang, K. N. et al. Bi-functional 3D-NiCu-Double hydroxide@partially etched 3D-NiCu catalysts for Non-Enzymatic glucose detection and the hydrogen evolution reaction. *ACS Appl. Mater. Interfaces*. **14**, 33013–33023. https://doi.org/10.1021/acsami.2c04471 (2022).
6. Li, Q. F., Chen, X., Wang, H., Liu, M. & Peng, H. L. Pt/MXene-Based flexible wearable Non-Enzymatic electrochemical sensor for continuous glucose detection in sweat. *ACS Appl. Mater. Interfaces*. **15**, 13290–13298. https://doi.org/10.1021/acsami.2c20543 (2023).
7. Ma, X. et al. Large-Scale wearable Textile-Based sweat sensor with high sensitivity, rapid response, and stable electrochemical performance. *ACS Appl. Mater. Interfaces*. **16**, 18202–18212. https://doi.org/10.1021/acsami.4c01521 (2024).
8. Wang, Y. X. et al. Boron-doped graphene quantum Dots anchored to carbon nanotubes as noble metal-free electrocatalysts of uric acid for a wearable sweat sensor. *ACS Appl. Nano Mater.* **5**, 11100–11110 (2022).
9. Xu, X., Dong, X., Li, D., Qi, M. & Huang, H. Pt nanoflowers as a highly effective electrocatalyst for glucose oxidation in abiotic glucose fuel cells. *ACS Appl. Mater. Interfaces*. **15**, 17969–17977. https://doi.org/10.1021/acsami.3c01689 (2023).
10. Yang, L. et al. Direct laser writing of the porous graphene foam for multiplexed electrochemical sweat sensors. *ACS Appl. Mater. Interfaces*. **15**, 34332–34342. https://doi.org/10.1021/acsami.3c02485 (2023).
11. Zhang, S. et al. Epidermal patch with biomimetic multistructural microfluidic channels for timeliness monitoring of sweat. *ACS Appl. Mater. Interfaces*. **15**, 469–478. https://doi.org/10.1021/acsami.2c17583 (2023).
12. Zhao, H., Zhang, L., Deng, T. & Li, C. Microfluidic sensing textile for continuous monitoring of sweat glucose at rest. *ACS Appl. Mater. Interfaces*. **16**, 19605–19614. https://doi.org/10.1021/acsami.4c01912 (2024).
13. Rdest, M. & Janas, D. Carbon nanotube wearable sensors for health diagnostics. *Sensors* **21**, 5847 (2021).
14. Mei, Z., Song, Y., Jiang, G., Wu, D. & Li, G. SnO2/ZnO/Ti3C2Tx MXene nanocomposites for highly sensitive and stable ethanol sensing at low temperature. *Sens. Actuators B*, 136390 (2024).
15. Wang, D. et al. Quantitative detection of multi-component chemical gas via MXene-based sensor array driven by triboelectric nanogenerators with CNN-GRU model. *Sens. Actuators B*, 136101 (2024).
16. Ferri, S., Kojima, K. & Sode, K. (SAGE, (2011).
17. Vashist, S. K., Zheng, D., Al-Rubeaan, K., Luong, J. H. & Sheu, F. S. Technology behind commercial devices for blood glucose monitoring in diabetes management: A review. *Anal. Chim. Acta*. **703**, 124–136 (2011).
18. Hwang, D. W., Lee, S., Seo, M. & Chung, T. D. Recent advances in electrochemical non-enzymatic glucose sensors–a review. *Anal. Chim. Acta*. **1033**, 1–34 (2018).
19. Heller, A. & Feldman, B. Electrochemical glucose sensors and their applications in diabetes management. *Chem. Rev.* **108**, 2482–2505 (2008).
20. Lucisano, J. Y., Routh, T. L., Lin, J. T. & Gough, D. A. Glucose monitoring in individuals with diabetes using a long-term implanted sensor/telemetry system and model. *IEEE Trans. Biomed. Eng.* **64**, 1982–1993 (2016).
21. Gough, D. A., Bremer, T. & Analysis Immobilized glucose oxidase in implantable glucose sensor technology. *Diabetes. Technol. Ther.* **2**, 377–380 (2000).
22. Kim, J. et al. Wearable smart sensor systems integrated on soft contact lenses for wireless ocular diagnostics. *Nat. Commun.* **8**, 1–8 (2017).
23. Liu, Q. et al. Highly sensitive and wearable In2O3 nanoribbon transistor biosensors with integrated on-chip gate for glucose monitoring in body fluids. *ACS Nano*. **12**, 1170–1178 (2018).
24. Nightingale, A. M. et al. Monitoring biomolecule concentrations in tissue using a wearable droplet microfluidic-based sensor. *Nat. Commun.* **10**, 1–12 (2019).
25. Nyein, H. Y. Y. et al. A wearable patch for continuous analysis of thermoregulatory sweat at rest. *Nat. Commun.* **12**, 1–13 (2021).
26. Park, S. J., Kim, M. H. & Ha, T. J. All-printed wearable humidity sensor with hydrophilic Polyvinylpyrrolidone film for mobile respiration monitoring. *Sens. Actuators B*. **394**, 134395 (2023).
27. Yang, Y., Lou, J., Qi, D. & Zhao, C. Flexible and transparent humidity sensors based on hyperbranched Poly (ionic liquid) s for wearable sensing. *Sens. Actuators B*. **404**, 135267 (2024).
28. Zhang, Q. et al. Smartphone-based plant-wearable microfluidic sensor with self driven electrolyte for in-situ detection of Methyl parathion. *Sens. Actuators B*, 136254 (2024).
29. Zhuang, Z., Xuan, X., Li, H., Jiang, D. & Li, M. A wearable antenna sensor based on ePDA/SiO2 nanowalls for the detection of lactic acid in sweat. *Sens. Actuators B*. **404**, 135265 (2024).
30. Shah, N. C., Lyandres, O., Walsh, J. T., Glucksberg, M. R. & Van Duyne, R. P. Lactate and sequential lactate – glucose sensing using surface-enhanced Raman spectroscopy. *Anal. Chem.* **79**, 6927–6932 (2007).
31. Steiner, M. S., Duerkop, A. & Wolfbeis, O. Optical methods for sensing glucose. *Chem. Soc. Rev.* **40**, 4805–4839 (2011).
32. Farahmandpour, M., Ansari, H. R. & Kordrostami, Z. Flexible Enzyme-Free gate engineered Bio-FET glucose sensor based on Nickel-Tungstate microcrystals. *IEEE Sens. J.* (2024).
33. Farahmandpour, M., Haghshenas, H. & Kordrostami, Z. Blood glucose sensing by back gated transistor strips sensitized by CuO Hollow spheres and rGO. *Sci. Rep.* **12**, 21872 (2022).
34. Farahmandpour, M., Dideban, D., Dehbali, M. M. & Kordrostami, Z. Disposable wireless FET paper sensor based on MWCNT/MXene/MoS2 composite for Non-Invasive glucose detection in saliva. *J. Alloys Compd.*, **178715** (2025).
35. Chakraborty, P., Dhar, S., Deka, N., Debnath, K. & Mondal, S. P. Non-enzymatic salivary glucose detection using porous CuO nanostructures. *Sens. Actuators B*. **302**, 127134 (2020).
36. Zhao, J. et al. A fully integrated and Self-Powered smartwatch for continuous sweat glucose monitoring. *ACS Sens.* **4**, 1925–1933. https://doi.org/10.1021/acssensors.9b00891 (2019).
37. Zhang, M. et al. Highly sensitive glucose sensors based on enzyme-modified whole-graphene solution-gated transistors. *Sci. Rep.* **5**, 8311 (2015).
38. Mehmood, T. et al. A flexible, printable, thin-film thermoelectric generator based on reduced graphene oxide–carbon nanotubes composites. *J. Mater. Sci.* **55**, 10572–10581 (2020).
39. Chen, L. et al. Superhydrophobic functionalized Ti3C2T X MXene-based skin-attachable and wearable electrochemical pH sensor for real-time sweat detection. *Anal. Chem.* **94**, 7319–7328 (2022).
40. Bhide, A., Muthukumar, S. & Prasad, S. CLASP (Continuous lifestyle awareness through sweat platform): A novel sensor for simultaneous detection of alcohol and glucose from passive perspired sweat. *Biosens. Bioelectron.* **117**, 537–545 (2018).
41. Yuan, Y., Wang, Y., Wang, H. & Hou, S. Gold nanoparticles decorated on single layer graphene applied for electrochemical ultrasensitive glucose biosensor. *J. Electroanal. Chem.* **855**, 113495 (2019).
42. Sempionatto, J. R., Moon, J. M. & Wang, J. Touch-based fingertip blood-free reliable glucose monitoring: personalized data processing for predicting blood glucose concentrations. *ACS Sens.* **6**, 1875–1883 (2021).
43. Chen, Y. et al. A wearable non-enzymatic sensor for continuous monitoring of glucose in human sweat. *Talanta* **278**, 126499 (2024).
44. Xiao, Y. et al. Noninvasive glucose monitoring using portable GOx-Based biosensing system. *Anal. Chim. Acta*. **1287**, 342068 (2024).
45. Lin, P. H., Sheu, S. C., Chen, C. W., Huang, S. C. & Li, B. R. Wearable hydrogel patch with noninvasive, electrochemical glucose sensor for natural sweat detection. *Talanta* **241**, 123187 (2022).
46. Barmpakos, D., Tsamis, C. & Kaltsas, G. Multi-parameter paper sensor fabricated by inkjet-printed silver nanoparticle ink and PEDOT: PSS. *Microelectron. Eng.* **225**, 111266 (2020).

47. Yan, Z. Y., Liu, J. Y. & Niu, J. R. Research of a novel ag temperature sensor based on fabric substrate fabricated by Magnetron sputtering. *Materials* **14**, 6014 (2021).
48. Hong, S. Y. et al. Stretchable active matrix temperature sensor array of polyaniline nanofibers for electronic skin. *Adv. Mater.* **28**, 930–935 (2016).
49. Harada, S. et al. Fully printed flexible fingerprint-like three-axis tactile and slip force and temperature sensors for artificial skin. *ACS Nano*. **8**, 12851–12857 (2014).
50. Zhou, L. et al. Liquid metal-doped conductive hydrogel for construction of multifunctional sensors. *Anal. Chem*. **95**, 3811–3820 (2023).
51. Yang, J. et al. Wearable temperature sensor based on graphene nanowalls. *RSC Adv.* **5**, 25609–25615 (2015).
52. Zhang, F. et al. Multi-modal strain and temperature sensor by hybridizing reduced graphene oxide and PEDOT: PSS. *Compos. Sci. Technol.* **187**, 107959 (2020).
53. Dankoco, M., Tesfay, G., Bènevent, E. & Bendahan, M. Temperature sensor realized by inkjet printing process on flexible substrate. *Mater. Sci. Engineering: B*. **205**, 1–5 (2016).
54. Manjakkal, L., Dang, W., Yogeswaran, N. & Dahiya, R. Textile-based potentiometric electrochemical pH sensor for wearable applications. *Biosensors* **9**, 14 (2019).
55. Zamora, M. L. et al. Potentiometric textile-based pH sensor. *Sens. Actuators B.* **260**, 601–608 (2018).
56. Mariani, F. et al. Design of an electrochemically gated organic semiconductor for pH sensing. *Electrochem. Commun.* **116**, 106763 (2020).
57. Choi, M. Y. et al. A fully textile-based skin pH sensor. *J. Ind. Text.* **51**, 441S–457S (2022).
58. Maiolo, L. et al. Flexible pH sensors based on polysilicon thin film transistors and ZnO nanowalls. *Appl. Phys. Lett.* 105 (2014).
59. Tang, Y. et al. Lattice proton intercalation to regulate WO3-based solid-contact wearable pH sensor for sweat analysis. *Adv. Funct. Mater.* **32**, 2107653 (2022).
60. Song, Y. et al. Wireless battery-free wearable sweat sensor powered by human motion. *Sci. Adv.* **6**, eaay9842 (2020).

Author contributions
M.F. and Z.K. designed and Fabricated Bio-OFETs sensors. All authors reviewed the manuscript.

Funding
This work in based upon research funded by Iran National Science Foundation (INSF) under project No. 4013206.

Declarations

Competing interests
The authors declare no competing interests.

Additional information
Supplementary Information The online version contains supplementary material available at https://doi.org/10.1038/s41598-025-00533-1.

Correspondence and requests for materials should be addressed to Z.K.